On the motion of small spherical bubbles in two-dimensional vortical flows

G. R. Ruetsch[a] and E. Meiburg[b]
Department of Aerospace Engineering, University of Southern California, Los Angeles, California 90089-1191

The motion of small, spherical noninteracting bubbles in two-dimensional vortical flows by means of numerical simulations is investigated. After a discussion concerning the various bubble equations, bubble trajectories are calculated in a solid-body vortex, where it is found that the bubble motion can be described in terms of the location where the bubbles accumulate, or equilibrium points, and the rate of entrapment into these equilibrium points. Of importance here is that the rate of entrapment into the vortex has an optimum value for some value of the inertia parameter, or inverse Stokes number. The bubble motion in a temporally evolving shear layer is investigated, where it is found that the solid-body vortex model predicts the trends in the growth in concentration about the vortex center for the case without gravity. For the case with gravity, not all bubbles are captured by the vortex, and the percentage of bubbles captured increases with decreasing inertia parameter. Also discussed is how these factors affect the generation of the interface between regions seeded and not seeded with bubbles.

I. INTRODUCTION

One of the fundamental applications of the study of shear flows concerns the ability to predict and model the transport of non-Lagrangian particles. Although much has been learned about the transport of heavy particles in shear layers, most recently through experiments by Lázaro and Lasheras[1,2] and computational simulations of Chung and Troutt,[3] the motion of bubbles in shear layers is less understood. One reason for this is the complexity of the equation of motion for bubbles. Maxey and Riley[4] have derived an equation for the motion of small spherical particles in an unsteady nonuniform flow field by assuming unsteady Stokes flow. Under certain circumstances, this equation can be used to calculate the trajectories of bubbles. Auton et al.[5] have taken a different approach, where they developed an equation for bubble motion assuming inviscid flow over the bubble. Despite the differences between these two approaches, both viscous and inviscid bubble equations result in the tendency of bubbles to accumulate in regions of low pressure, e.g., the center of vortices. The entrapment of Stokes bubbles in vortices has been found in simulations with cellular flow fields by Maxey and Corrsin[6] and Maxey.[7] The entrapment of bubbles in a modified Rankine vortex has been investigated analytically for small Stokes number by Tio et al.[8] Similar entrapment features for inviscid bubbles in isolated vortices and shear layers have been found in simulations by Hunt et al.[9] and Thomas et al.[10]

In this study, we further explore the accumulation of bubbles in both isolated vortices and shear layers. After discussing the equation for viscously dominated bubble motion, we examine the trajectories of these bubbles in an isolated vortex, namely a fluid in solid-body rotation. For this simple flow, the trajectories can be calculated analyt-

ically, where an optimum entrapment rate in terms of the ratio of viscous to inertial forces is found. We then relate the characteristics found in this simple flow to bubble motion in a temporally evolving shear layer.

II. BUBBLE EQUATION AND DYNAMICS

The motion of bubbles can be examined in a variety of different regimes, and before we begin our analysis of bubble motion, it is necessary to consider which regimes we wish, and are able, to pursue. We need to discuss the equations of motion, the conditions under which they are valid, and their completeness. To simplify our analysis, we wish to consider as a first step only passive bubbles, i.e., bubbles that do not affect either the surrounding fluid or other bubbles. We would also like to consider a simple geometry for bubbles, namely that they are spherical and incompressible. These assumptions about the passive nature and geometrical properties occur in flows where the length scale of the bubble is small compared to the flow length scale, when the bubble concentration is dilute, and when a large surface tension exists which keeps the spherical shape.

The final characteristic we consider is to determine what role the drag forces play. There are two different approaches we can use here. One approach is to assume the flow around the bubble to be inviscid and then to add a drag term in the equation. This approach has been used to develop the equation of motion for an inviscid bubble by Auton et al.[5] The second approach is to consider bubbles which are dominated by viscous forces. Small bubbles with surface impurities fall into this category.[11] In this study we use the latter approach, which is discussed in more detail in the following section.

A. Stokes limit

We shall begin by considering particles that obey the Stokes drag law using the equation for small rigid spheres developed by Maxey and Riley.[4] This equation is applica-

ble to small spherical particles at low Reynolds numbers and is valid for a the full range of particle densities, ranging from aerosols to bubbles. A simplified version of this equation which neglects the Faxen corrections for a nonuniform flow field gives

$$m_p \frac{d\mathbf{V}}{dt} = (m_p - m_f)\mathbf{g} + m_f \frac{D\mathbf{u}}{Dt}\bigg|_{\mathbf{Y}(t)} + \frac{1}{2} m_f \frac{d}{dt} [\mathbf{u}(\mathbf{Y},t)$$
$$ - \mathbf{V}(t)] + 6\pi a\mu [\mathbf{u}(\mathbf{Y},t) - \mathbf{V}(t)]$$
$$ + 6\pi a^2 \mu \int_0^t \frac{d(\mathbf{u}-\mathbf{V})/d\tau}{\sqrt{\pi\nu(t-\tau)}} d\tau, \qquad (1)$$

where $\mathbf{u}(\mathbf{x},t)$ is the fluid velocity, $\mathbf{Y}(t)$ and $\mathbf{V}(t)$ are the particle location and velocity, $\mathbf{g}$ is the acceleration of gravity, a is the particle radius, and m_p and m_f are the particle mass and the mass of the fluid displaced by the particle. Equation (1) states that the particle experiences an acceleration due to, respectively, a buoyancy force, the force a fluid sphere of the same size would experience in absence of the particle, the added mass effect, Stokes drag, and the Basset history term. This leading order approximation, where Stokes flow is assumed, does not contain the Saffman lift force.[12] Bretherton[13] has shown that under the assumption of Stokes flow, spherical particles cannot exhibit such a lateral motion or "migration." As noted in Maxey and Riley's paper it is important to differentiate between the two derivatives in Eq. (1). The derivative following a fluid element is denoted as

$$\frac{D}{Dt} = \frac{\partial}{\partial t} + \mathbf{u} \cdot \nabla,$$

whereas the derivative along the particle path is

$$\frac{d}{dt} = \frac{\partial}{\partial t} + \mathbf{V} \cdot \nabla.$$

In deriving Eq. (1), the force on the sphere was evaluated by separating the flow field into two components, the undisturbed and disturbance flows. In order to obtain the force on the sphere due to the undisturbed flow, the particle radius must be small compared to flow length scale, L, or $a/L \ll 1$. In order to obtain the force due to the disturbance flow the convective terms were neglected, implying Stokes flow, which requires the particle Reynolds number based on the slip velocity to be small:

$$R_p = 2a|\mathbf{u}-\mathbf{V}|/\nu \ll 1, \qquad (2)$$

and in addition,

$$\left(\frac{a}{L}\right)^2 R_f \ll 1, \qquad (3)$$

where $R_f = UL/\nu$ is the Reynolds number for the main flow based on the characteristic velocity scale U. As long as $a/L \ll 1$, R_f can be large up to $O(L/a)$ while Eq. (2) is still satisfied. We should state here that in this paper we consider bubbles where Eq. (3) is not satisfied. As a result we will modify terms in Eq. (1) accordingly. Along these lines, we can eliminate the Basset history term from Eq. (1), as the departure from Stokes flow lessens the history

effect. This has been documented in Mei et al.,[14] where they find that the kernel behaves as $t^{-1/2}$ only for short times and decays faster at large time for finite Reynolds numbers.

Rearranging terms in Eq. (1) and removing the Basset history term, we have

$$\left(m_p + \frac{1}{2} m_f\right) \frac{d\mathbf{V}}{dt} = (m_p - m_f)\mathbf{g} + 6\pi a\mu [\mathbf{u}(\mathbf{Y},t)$$
$$ - \mathbf{V}(t)] + m_f \left(\frac{D\mathbf{u}}{Dt} + \frac{1}{2} \frac{d\mathbf{u}}{dt}\right), \qquad (4)$$

where nondimensionalizing with respect to L as length, U as velocity, L/U as time, and using the notation of Maxey[7,15] results in

$$\frac{d\mathbf{V}}{dt} = A[\mathbf{u}(\mathbf{Y},t) + \mathbf{W} - \mathbf{V}(t)] + R\left(\frac{D\mathbf{u}}{Dt} + \frac{1}{2} \frac{d\mathbf{u}}{dt}\right). \qquad (5)$$

Three nondimensional parameters are introduced in Eq. (5): A, R, and $\mathbf{W}$. The scaled particle settling velocity, $\mathbf{W}$, is defined as

$$\mathbf{W} = \frac{(m_p - m_f)\mathbf{g}}{6\pi a\mu U}. \qquad (6)$$

and reflects the gravitational effects on the particle motion. Physically, $\mathbf{W}U$ is the terminal velocity of a particle in a still fluid.

Also in Eq. (5) is the mass ratio parameter, R, given by

$$R = \frac{\rho_f}{\rho_p + \frac{1}{2}\rho_f}, \qquad (7)$$

which determines the type of particle, with values ranging from $0 \leqslant R \leqslant 2$. Aerosol particles typically exist in the range of $0 < R \leqslant 0.4$, and at the other end of the range is the bubble limit, where $R = 2$.

The inertia parameter, A, is defined as

$$A = \frac{6\pi a\mu L}{(m_p + \frac{1}{2}m_f)U} = \frac{9}{2} R \left(\frac{L}{a}\right)^2 \frac{1}{R_f} \qquad (8)$$

and indicates the importance of viscous effects relative to the particle inertia; the smaller A the more important particle inertia. The inverse of the inertia parameter is commonly referred to as the Stokes number. Physically, the first term on the right-hand side in Eq. (5) influences the particle velocity to match the sum of fluid and settling velocities, or simply the fluid velocity if $\mathbf{W} = 0$. From Eq. (3) we obtain the condition that

$$A \gg \frac{9}{2} R \qquad (9)$$

which in the case of bubbles leads to $A \gg 9$. This gives a criterion for when inertial effects become important, and, therefore, when the Stokes drag is no longer valid. This restriction can be relaxed by applying the empirical multiplicative factor, f_1, to the term $A(\mathbf{u}-\mathbf{V})$ in Eq. (5) given by Clift et al.:[11]

$$f_1 = 1 + 0.1315 R_p^{(0.82 - 0.05 \log R_p)} \qquad (10)$$

which accounts for the effect of the wake behind the sphere on the drag and extends the range of validity to $R_p < 20$.

With the nondimensional parameters in Eq. (5) defined, we will now turn attention to the physical processes which occur. The drag term in Eq. (5) causes the particle velocity to conform to the local fluid and settling velocity, the degree of which depends on the value of A. In terms of particle size, smaller particles will have a larger inertia parameter and a smaller settling velocity, which implies that smaller particles will follow the fluid more closely than larger particles. The remaining terms which are preceded by the mass ratio parameter have their origin in two different physical phenomena. The derivative following a fluid element can be rewritten using the Navier–Stokes equation,

$$\frac{D\mathbf{u}}{Dt} = -\nabla P + \frac{1}{R_f} \nabla^2 \mathbf{u}, \qquad (11)$$

which further emphasizes that this term represents the force that a fluid element would experience in place of the particle. The fluid velocity derivative following the particle path comes from the added mass term. Rewriting this in terms of the material derivative gives

$$\frac{d\mathbf{V}}{dt} = f_1 A(\mathbf{u} - \mathbf{V}) + A\mathbf{W} + R\left(\frac{3}{2}\frac{D\mathbf{u}}{Dt} + \frac{1}{2}(\mathbf{V} - \mathbf{u}) \cdot \nabla \mathbf{u}\right). \qquad (12)$$

Note the 3/2 coefficient of the pressure term. If $R = 2/3$ and if the initial particle velocity is that of the local fluid, Eq. (12) reduces to

$$\frac{d\mathbf{V}}{dt} = \frac{D\mathbf{u}}{Dt}, \qquad (13)$$

implying the particle moves with the fluid, i.e., the particle is a Lagrangian particle, regardless of the value of A. The viscous forces do not act since the slip velocity remains zero. For bubbles, where $R = 2$, the pressure gradients are felt three times as much as in the case of fluid elements. This extra sensitivity to pressure effects plays a dominant role in the dynamics of bubbles, causing the bubbles to accumulate in regions of low pressure.

Previously we mentioned that a particle in Stokes flow does not experience a Saffman lift force. More generally, velocity shear cannot produce any force for this linearized flow. However, by writing the last term of Eq. (12) as follows:

$$\frac{1}{2}(V_j - u_j)\frac{\partial u_i}{\partial x_j} = \frac{1}{2}(V_j - u_j)(R_{ij} + S_{ij})$$

$$= \frac{1}{4}\epsilon_{ijk}(u_j - V_j)\omega_k + \frac{1}{2}(V_j - u_j)S_{ij}, \qquad (14)$$

where S_{ij} and R_{ij} are the rate of strain and rate of rotation tensors, we do obtain forces from shearing motion. The first term is an inviscid lift force based on the slip velocity,

and the second term allows for the amplification and tilting of the slip velocity, in the same manner that a vorticity vector is stretched and tilted in the three-dimensional vorticity equation.[16] The lift force in Eq. (14) is quite different from the Saffman lift, because the former is inviscid and proportional to the vorticity, and the later is dependent on viscosity and proportional to the square root of the vorticity. The presence of such terms might appear contradictory given the nature of Stokes flow, however, we must keep in mind the assumptions under which this particle equation is derived. Maxey and Riley show that the terms in Eq. (14), in the context of the low Reynolds number approximations made, are of the same order as other terms neglected in deriving Eq. (1). Put another way, in order to satisfy Eq. (9) the viscous forces must be dominant so as to keep the slip velocity small enough so that the terms in Eq. (14) are negligible.

In this paper, however, we consider cases where the inertia and viscous effects are comparable, i.e., $A \sim 1$. We have modified the Stokes drag term by using the empirical result in Eq. (10) to compensate for this fact, however, no such corrections are currently available for the other terms. At this point, it is helpful to look at the differences between the governing equations for bubble motion in the Stokes and inviscid limits. In addition to the absence of a viscous force, the inviscid bubble equation differs from the Stokes equation in other respects. Auton et al.[5] showed that for inviscid bubbles, the added mass derivative is $D\mathbf{u}/Dt$ instead of $d\mathbf{u}/dt$. In addition to the added mass derivative, there is also an inviscid lift force which is proportional to $(\mathbf{u} - \mathbf{V}) \times \omega$ and twice as large as the lift term in Eq. (14). In this study we make no attempt to determine which approach is more valid at this "intermediate" range, however we do attempt to gain insight into what effect using different terms in the bubble equation has on the overall features of the bubble motion. We do this in the next section, where analytical solutions for the bubble trajectories in a solid-body vortex are obtained using both $d\mathbf{u}/dt$ and $D\mathbf{u}/Dt$ as added mass derivatives.

III. BUBBLES IN A SOLID-BODY VORTEX

In this section we analyze bubble motion in steady, isolated vortices. In particular, we consider the motion of the bubbles in a solid-body vortex, where the fluid velocity can be expressed in polar coordinates as

$$u_\vartheta = \frac{\omega_0}{2} r. \qquad (15)$$

The reason for using this type of flow field is twofold. First, the bubble equations simplify under such flows, which allows a closer examination of the effect of the individual terms in the governing equations. Second, circular vortices with a core of near constant vorticity can be thought of as an approximation to the final stages of a mixing layer. Also, studying the effect of a vortex on bubbles is essential for designing turbulence models for two-phase flows.

For the case of solid-body rotation, the flow itself has no length or velocity scale. Therefore, we use $T = 1/\omega_0$,
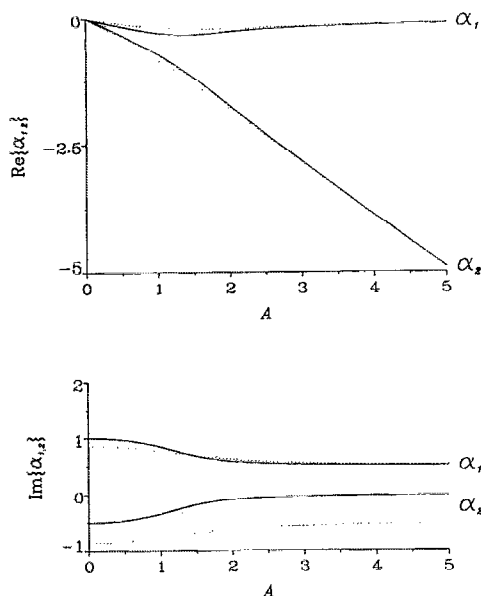
2328   Phys. Fluids A, Vol. 5, No. 10, October 1993

G. R. Ruetsch and E. Meiburg   2328

FIG. 1. Exponents for the trajectories of Stokes bubbles. Here the two different added mass fluid velocity derivatives are used: Du/Dt ($\cdots$) and du/dt (—). The optimum entrapment occurs at $A=1.34$ with $\mathrm{Re}(\alpha_1)=-0.32$ when du/dt is used as the added mass fluid derivative, and occurs at $A=1.58$ with $\mathrm{Re}(\alpha_1)=-0.21$ when Du/Dt is used as the added mass fluid derivative.
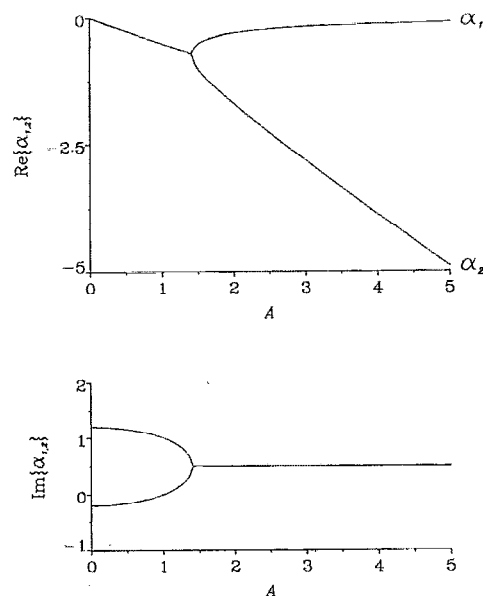
FIG. 2. Exponents for the trajectories of bubbles using Du/Dt as the added mass derivative and the inviscid Auton lift effect. The optimum entrapment rate occurs at $A_c=\sqrt{2}$ with $\mathrm{Re}(\alpha_c)=-1/\sqrt{2}$. For $A<A_c$ both exponents have the same real component given by $\mathrm{Re}(\alpha)=-A/2$.

$L=r_0$, and $U=r_0\omega_0$ as the time, length, and velocity scales, where r_0 is the initial bubble position and ω_0 is the vorticity. Using this scaling gives the nondimensional vorticity and velocity as $\omega_z=1$ and $u_\vartheta=r/2$.

For the case of a viscous bubble, an analytical solution for the bubble trajectory can be obtained if we assume a Stokes drag law, i.e., $f_1=1$. In order to illustrate the contribution, or lack thereof, of the terms in Eq. (14) to the solution, we will calculate the solution using both Du/Dt and du/dt as the added mass fluid velocity derivatives. For a solid-body vortex, the term $(V_j-u_j)S_{ij}$ is zero, so that the only difference between the two added mass derivatives in this case is the term $\frac{1}{2}\epsilon_{ijk}(u_j-V_j)\omega_k$. This allows us to evaluate what effect a lift force has on the bubble motion. In addition, we will also briefly consider the case where Du/Dt is used along with the inviscid lift effect given by Auton et al.[5] which is twice that of Eq. (14). For all versions, the general solution is

$$X(t)-X_E=a_1\exp(\alpha_1 t)+a_2\exp(\alpha_2 t)+\text{c.c.},\qquad(16)$$

$$Y(t)-Y_E=b_1\exp(\alpha_1 t)+b_2\exp(\alpha_2 t)+\text{c.c.}\qquad(17)$$

In terms of entrapment characteristics, the two main important features given by this solution are the equilibrium points, (X_E,Y_E), and the rate of entrapment, given by the real components of α_1 and α_2. The exponents α_1 and α_2 are functions of A alone, and both the real and imaginary components are shown in Fig. 1, where solutions using the two different added mass derivatives are shown. In general, and especially for large A, the results do not depend heavily on which added mass derivative is used. The only large discrepancy is in the frequency of the α_2 term. Since $\mathrm{Re}\{\alpha_2\}<\mathrm{Re}\{\alpha_1\}$, however, this frequency is associated

with a larger decay rate and, hence, represents only transient behavior. In addition, the period of oscillation associated with α_2 becomes infinite for large A. Actually, when Du/Dt is used as the added mass derivative, there is only one frequency, with $\mathrm{Im}(\alpha_1)=-\mathrm{Im}(\alpha_2)$. By using the added mass form in Maxey and Riley, we introduce a small lift effect which creates an additional frequency.

One important feature of the solutions represented in Fig. 1 is that the long term motion has an optimal entrapment rate, signified by the minimum in $\mathrm{Re}(\alpha_1)$. When Du/Dt is used as the added mass derivative, this optimum entrapment occurs at $A_c=1.58$ with $\mathrm{Re}(\alpha_1)=-0.21$. When du/dt is used as the added mass derivative, the location and value are shifted to $A_c=1.34$ and $\mathrm{Re}(\alpha_1)=-0.32$. This difference is a result of the lift effect in Eq. (14), which causes the greater entrapment rate to occur at smaller A. The addition of more lift does not guarantee that this trend continues, which is observed if we use Du/Dt along with the Auton inviscid lift effect, which amounts to twice the lift contained in du/dt. Although the magnitude of the optimum entrapment is greater for this case than the other cases, where $\mathrm{Re}(\alpha_1)=-1/\sqrt{2}\sim-0.71$, the location occurs between the two previous cases, at $A_c=\sqrt{2}\sim1.4$. For this case the exponents take on a slightly different characteristic, as indicated in Fig. 2. This is a limiting case which for $A<A_c$ the real component of both exponents is the same, given by $\mathrm{Re}(\alpha)=-A/2$, and for $A>A_c$ there is only one frequency. However, we should remember that this solution is for the case where we use an inviscid lift term with a Stokes drag.

The information given by the analytical solution can be put into context by examining typical bubble trajectories. Several trajectories are shown in Fig. 3 for various values of A. Here the local fluid velocity is used as an initial
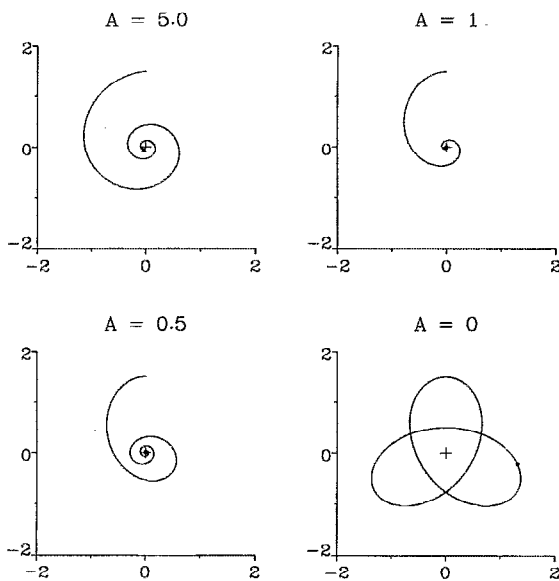
FIG. 3. Stokes bubble trajectories for various A. Here $d\mathbf{u}/dt$ is used as the added mass derivative.
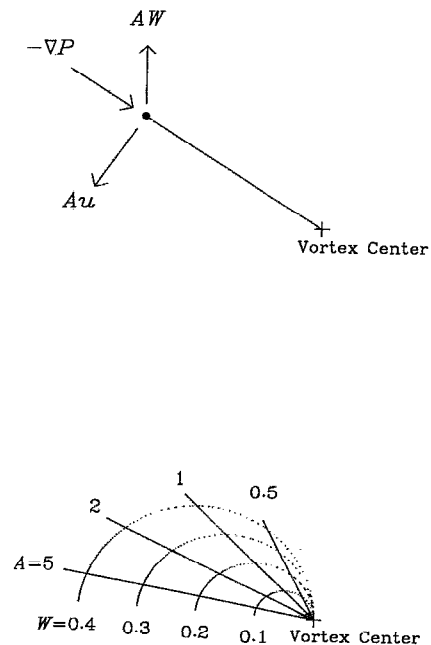

FIG. 4. Force balance (top) and location (bottom) of equilibrium points as a function of A and W for a solid-body vortex. For large A the equilibrium point shifts towards the horizontal axis as the balance is primarily between the drag and gravitational forces. For smaller A the pressure forces become more important as the equilibrium point moves upwards. For any values of A and W there always exists an equilibrium point.

condition for the bubble velocity, and $d\mathbf{u}/dt$ is taken as the added mass derivative. In cases where A is large, the viscous forces dominate and inhibit the radial motion, so that the larger A, the more circular the trajectories. As A decreases towards A_c, the radial velocity component becomes larger as the bubble moves more quickly towards the vortex center. However, for $A < A_c$ the bubble once again approaches the vortex center more slowly. In addition to this slower asymptotic entrapment rate, there is also an initial "overshoot" past the vortex center. This phenomenon has been observed in a similar way in dispersion models for heavy particles in vortical flows.[17] This reflects the tendency of heavy particles to spiral out of vortices, since in their case $R=0$ and therefore the pressure forces have no effect. The dynamics for the bubble "overshoot," on the other hand, is quite different. The radial motion of the bubbles is dominated primarily by two forces, the inward pressure gradient force and the outward added mass effects. Neglecting the drag and lift forces, the balance between the pressure gradient and added mass effects occurs when $V_\vartheta/u_\vartheta = \sqrt{3}$, since the bubbles are three times more sensitive to the pressure gradient than fluid elements. Note that this criterion is dependent on both the bubble and local fluid velocities. The drag force generally maintains $V_\vartheta/u_\vartheta \sim 1$, which results in the inward radial motion of the bubbles. However, for a bubble with small A, both radial and azimuthal bubble velocities can become large. An increase in both of these bubble velocity components contributes to an increase in V_ϑ/u_ϑ, since as the radial bubble velocity becomes larger the bubble is convected into regions of smaller u_ϑ. This latter effect is dependent on $u_\vartheta(r)$, or the "shape" of the vortex. As a result, when A becomes small enough, V_ϑ/u_ϑ can exceed $\sqrt{3}$ and an outward acceleration can exist. Note that this argument neglects the effect of the lift and drag forces on the radial motion, however, adding these contributions does not qual-

itatively affect this mechanism. It should be emphasized that this "overshoot" is a transient feature and is not responsible for the smaller asymptotic rate of entrapment.

Although the rate of entrapment is a function of A alone, the equilibrium points depend on both A and $\mathbf{W}$. When $d\mathbf{u}/dt$ is used as the added mass derivative the equilibrium points are defined by

$$X_E = -\frac{2A^2 W}{1+A^2},$$

$$Y_E = \frac{2AW}{1+A^2}. \tag{18}$$

These equilibrium points occur where there is a balance between the drag, gravity and pressure forces, as indicated in Fig. 4. For the case of the viscous added mass derivative, the inward pressure forces are reduced by the previously mentioned lift forces. Also shown in Fig. 4 are loci of points which indicate the location of the equilibrium points in terms of the parameters A and W. When $W=0$ the equilibrium point lies on the vortex center, and as W becomes larger the equilibrium points moves along a straight line away from the vortex center. The slope of this line depends on the value of A. For large A this line is roughly horizontal, indicating a primary balance between the gravity and viscous forces. For smaller values of A this line becomes more vertical as the pressure force become more important in the force balance. As with the rate of entrapment, the equilibrium points change when $D\mathbf{u}/Dt$ is used as the added mass derivative. These equilibrium points are given by
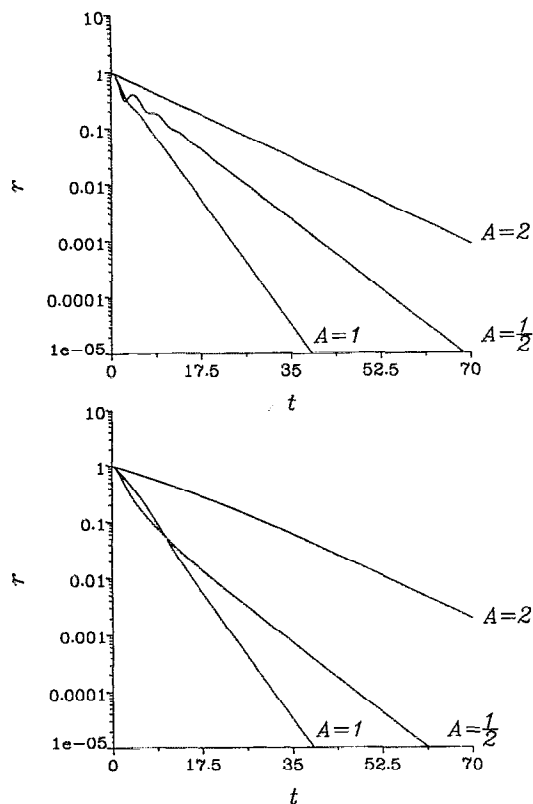
FIG. 5. Bubble radius time series without (top) and with (bottom) the drag modification factor. The long term decay rate is not affected by the drag modification.
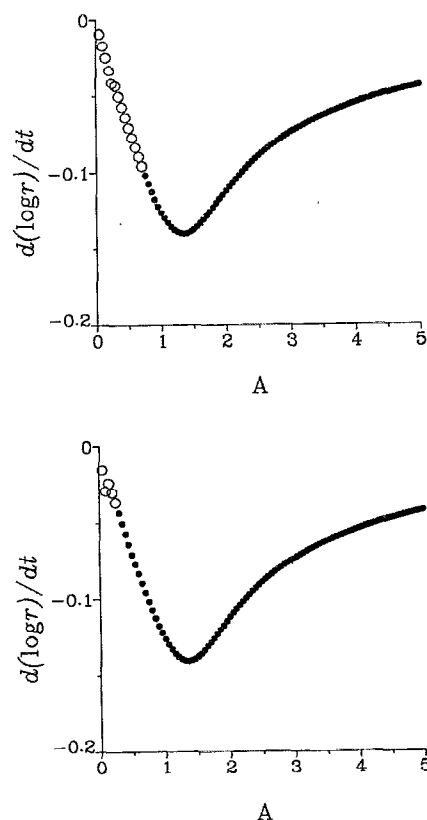

FIG. 6. Long term radial decay of bubbles without (top) and with (bottom) drag modification. The hollow circles represent bubbles where local maximum radial positions were observed, and filled circles indicate monotonically decreasing radial position.

$$X_E = -\frac{8A^2W}{9+4A^2},\qquad (19)$$

$$Y_E = \frac{12AW}{9+4A^2},\qquad (20)$$

and though different from the case using the viscous added mass term, the characteristics are roughly the same.

For the range of A discussed so far, we have violated the condition in Eq. (9) for using the Stokes drag law, but we can correct this by using the empirical coefficient in Eq. (10), which is dependent on the particle Reynolds number. The factor has a weak dependence on R_p, and except for the cases of very small A, the characteristics found earlier without this factor are still valid. The particle Reynolds number is given by $R_p = (Ud/\nu)(|\mathbf{u}-\mathbf{V}|/U)$, in which case we must specify the additional parameter Ud/ν. For a shear flow with a velocity scale of 1 m/sec, a bubble diameter of 100 μm, and a kinematic viscosity of 10^{-6} m^2/sec, we obtain $Ud/\nu = 100$, which will be used throughout this study. This is most likely to be a globally turbulent flow since the global flow scale is >100 μm.

We begin the analysis with drag correction for cases without any gravitational effects, so that the equilibrium point lies on the vortex center. One method of evaluating the difference between the cases with and without drag correction is to plot time series of the bubbles' radial distance from the vortex center. This is shown in Fig. 5 for

different A, both with and without the drag correction factor. Here we can more clearly see the "overshoots" for the case of $A = 0.5$ without the drag correction, and their absence when the drag correction is applied. For this case, the maximum bubble Reynolds number is $R_p \sim 27$ with a corresponding value of $f_1 \sim 2.5$. We can also see from the slopes of the curves in Fig. 5 that an optimum entrapment occurs which is related to the minimum in the real component of α_1. This is further seen by plotting the final slope of the radial time series versus A in Fig. 6, again for cases with and without the drag correction. Here the filled circles represent trajectories where there are no local maxima in the radial position, whereas the hollow circles represent trajectories where there is at least one local maximum in the radial position. The only major difference caused by the drag correction is whether or not an early oscillatory state is present, but the asymptotic state is the same. The equivalent asymptotic states are a result of the flow conditions at the equilibrium point. When the equilibrium point coincides with the vortex center, which is the case when $W=0$, the value of the slip velocity and therefore the bubble Reynolds number is zero, so that there is no drag correction at the equilibrium point. A better assessment of the effects of the drag correction can be shown by considering more transient features of the bubble motion. Such an example is given in Fig. 7, where the value of A for the bubble with the

FIG. 8. Rate of entrapment for cases with a rise velocity and drag modification. The minimum in the curves shifts towards smaller A for larger rise velocities, due to the increased slip velocity and drag correction.
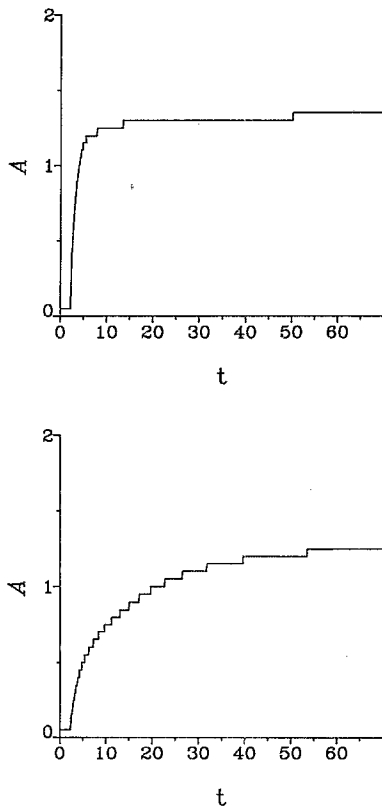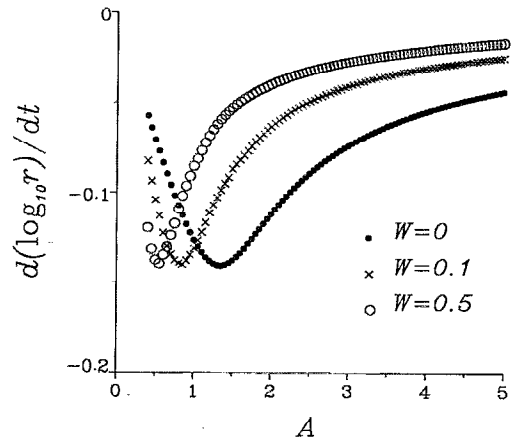
FIG. 7. The value of A for the bubble closest to the vortex center versus time for bubbles without (top) and with (bottom) drag modification. Initially the nearly inviscid bubbles are closest due to the lack of resistance to inward motion, however these bubbles overshoot the center. The final state corresponds to the minimum in Fig. 6. This transition is slower with drag modification.

minimum radial position is given for all times, again with and without drag correction. Here the final values are predicted by the analytical solution, and correspond to Fig. 6. However, at earlier times the bubbles closest to the vortex center are those with smaller A, where the inward motion is not restrained. As time progresses, these bubbles "overshoot" the vortex center and the more viscous bubbles become closest to the vortex center. This transition is quicker without the drag correction. With drag correction the "overshoots" for the less viscous bubbles are restrained and hence the minimal radial position stays longer with these bubbles. Thus in the early stages the entrapment rate increases with decreasing A.

Now we consider the effect of drag correction with gravitational effects. In doing so, it is useful to define a quantity f_{1E} as the value of the drag correction factor at the equilibrium point using the local fluid velocity as the slip velocity. Using this expression, the equilibrium points are given by

$$X_E = -\frac{2 f_{1E} A^2 W}{1 + (f_{1E} A)^2},$$

$$Y_E = \frac{2 A W}{1 + (f_{1E} A)^2},$$

(21)

where A and W from Eq. (18) have been replaced by $f_{1E} A$ and W/f_{1E}, respectively. The effect this has is to move the equilibrium point closer to the vortex center. In addition to the different location of the equilibrium points, the rate of entrapment also differs if we include drag correction. This is seen in Fig. 8, where the asymptotic entrapment rate is given versus A for different values of W. Here we see that as W increases, the maximum rate of entrapment shift towards smaller values of A. As with the location of the equilibrium points, this can be explained using the quantity f_{1E}. If we were to plot the entrapment rate versus $f_{1E} A$, the curves in Fig. 8 collapse. Therefore, as gravitational effects become more important and the equilibrium points move farther away from the vortex center, the maximum asymptotic entrapment rate moves towards smaller values of A. Note that even though the drag correction allows us to extend the valid range of A to smaller values, this approach still fails for very small A, and therefore for large W we cannot comment on the existence of a maximum entrapment rate.

IV. BUBBLES IN A SHEAR LAYER

A. Flow simulation

To this point we have analyzed bubble motion in steady isolated vortices. Before we discuss the motion of bubbles in a shear layer, we will briefly review the method used for obtaining the time-dependent flow field. Assuming the flow to be both unsteady and incompressible and the fluid as inviscid, the governing equations for the flow field are

$$\frac{D\omega}{Dt} = 0,$$

(22)

$$\nabla \cdot \mathbf{u}(\mathbf{x}, t) = 0.$$

(23)

The instantaneous velocity field can be obtained from the vorticity field in a flow governed by Eqs. (22) and (23) by solving the Poisson equation:

$$\nabla^2 \mathbf{u} = -\nabla \times (\omega \hat{\mathbf{e}}_z), \tag{24}$$

whose solution is given by the Biot–Savart equation,

$$\mathbf{u}(\mathbf{x},t) = -\frac{1}{2\pi} \int \frac{(\mathbf{x}-\mathbf{x}') \times \hat{\mathbf{e}}_z \omega(\mathbf{x}',t)}{|\mathbf{x}-\mathbf{x}'|^2} \, d\mathbf{x}'. \tag{25}$$

Although it is difficult to obtain solutions to Eq. (25) in general, approximations concerning the vorticity field can reduce Eq. (25) to a workable form. Such approximations are employed in the vortex blob method, which is used here to solve Eq. (25) and is thoroughly described in Leonard[18] and Nakamura et al.[19] This method discretizes the vorticity field into vortex blobs:

$$\omega(\mathbf{x},t) = \sum_{i=1}^{N} \Gamma_i \gamma_i(\mathbf{x}-\mathbf{x}_i), \tag{26}$$

where Γ_i is the circulation, or strength, of the ith blob and γ_i is the distribution, or smoothing function, of the vorticity about the center $\mathbf{x}_i$ of the ith blob. The vorticity distribution is also normalized, so

$$\int \gamma_i(\mathbf{x}) d\mathbf{x} = 1. \tag{27}$$

In this study a Gaussian distribution of vorticity is used, i.e.,

$$\gamma_i(\mathbf{x}-\mathbf{x}_i) = (1/\pi\sigma_i^2) \exp(-|\mathbf{x}-\mathbf{x}_i|^2/\sigma_i^2), \tag{28}$$

where σ_i is the core radius of the ith blob and indicates the concentration of the vorticity. For a shear layer simulation, vortex blobs with equal Γ_i and σ_i are evenly spaced on the x axis and then given a small initial sinusoidal perturbation to the circulation Γ_i used to initiate the Kelvin–Helmholtz instability. This perturbation is periodic in the $\pm x$ directions with period l. Although the vorticity field is discretized into many blobs for computational purposes, physically one must consider their collective effect. If the spacing between blobs is small, such a configuration with blob distributions given by Eq. (28) yields the velocity profile

$$U_0(y) = \tfrac{1}{2} \, \mathrm{erf}(y/\sigma_i). \tag{29}$$

In this study Γ_i is chosen so that $\Delta U_0 = 1$, and σ_i so that the maximum slope thickness,

$$\Theta_{ms} \equiv \Delta U_0 \bigg/ \left(\frac{du}{dy}\right)_{\max} = 1.0. \tag{30}$$

This also corresponds to an initial maximum vorticity of 1.0. Substituting Eqs. (26) and (28) into Eq. (25) then gives the velocity field due to the infinite series of vortex blobs. However, by considering all images except the closest image of a blob as point vortices, where $\gamma_i(\mathbf{x}) = \delta(\mathbf{x})$, and only the closest image of a blob as having the distribution given in Eq. (28), the following analytical expressions are obtained for the velocity fields:[19]

$$u(x,y) = \sum_{i=1}^{N} \left[\frac{y-y_i}{2\pi r_i^2} \Gamma_i \exp\left(-\frac{r_i^2}{\sigma_i^2}\right) \right.$$
$$\left. - \frac{\Gamma_i \sinh[k_0(y-y_i)]}{2l\{\cosh[k_0(y-y_i)] - \cos[k_0(x-x_i)]\}} \right], \tag{31}$$

$$v(x,y) = \sum_{i=1}^{N} \left[-\frac{x-x_i}{2\pi r_i^2} \Gamma_i \exp\left(-\frac{r_i^2}{\sigma_i^2}\right) \right.$$
$$\left. - \frac{\Gamma_i \sin[k_0(x-x_i)]}{2l\{\cosh[k_0(y-y_i)] - \cos[k_0(x-x_i)]\}} \right], \tag{32}$$

where $r_i = |\mathbf{x}-\mathbf{x}_i|$ and $k_0 = 2\pi/l$. For each i, the last term on the right-hand side of Eqs. (31) and (32) represents the velocity induced from the ith vortex and its periodic images as if they were point vortices, and the first term on the right-hand side is the vortex blob correction for the nearest image. This "hybrid" scheme combines the smooth, or nonsingular, characteristics of the vortex blob, when needed, with the simplicity of the point vortices, which allows the use of the analytical expression for the effect of all the images.

The temporal evolution of the flow is obtained by calculating the velocity at the blob centers, using Eqs. (31) and (32), and using a second-order predictor–corrector scheme to advance the blob centers. In the shear layer flow, where we simulate the trajectories of many particles, it is important to develop an efficient method of calculating the bubble trajectories. A detailed explanation and accuracy analysis of this method is given in the Appendix. To summarize, one must be careful how the fluid velocity derivatives from the added mass and pressure gradients are evaluated in order to maintain accuracy and do so efficiently. Using a first-order forward Euler scheme at the predictor step and a first-order backward Euler scheme at the corrector step to calculate the fluid velocity derivatives results in an overall second-order accurate scheme. In addition, the fluid velocity at the bubble location is not directly calculated using the Biot–Savart law, but instead the fluid velocities are calculated on a grid, and then a 2-D fourth-order Lagrange polynomial is used to interpolate the velocity at the bubble locations. This grid is initially 50×50 and occupies a region of $l \times l$.

B. Bubbles in a shear layer without gravity

We now turn our attention to the study of the motion of viscous bubbles in a temporally evolving shear layer. This shear layer, simulated using the vortex method discussed in the previous section, is given an initial perturbation to the blob circulation which corresponds to the most unstable mode obtained from stability theory.[20] The initial condition given to the bubbles is to seed the upper half of the shear layer with 12 000 bubbles equally spaced, resulting in a uniform concentration, and placed from the center of the shear layer out to $3\Theta_{ms}$. These bubbles are given an initial velocity equal to that of the fluid. We consider four
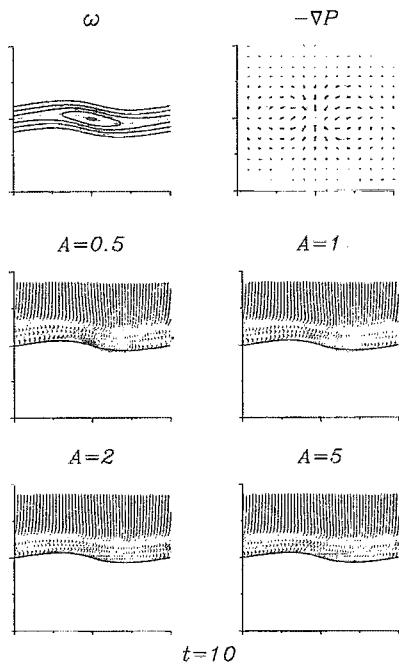
FIG. 9. Vorticity contours, pressure gradient field, and bubble positions at $t=10$. The solid line in the bubble figures represents the material line that was initially the centerline. Each graph represents one period in each direction.

FIG. 10. Vorticity contours, pressure gradient field, and bubble positions at $t=18$. Here the stronger pressure gradients cause the accumulation of bubbles at the vortex center.

different values of A, ranging from $A=0.5$ to $A=5$. For all cases we use Eqs. (5) and (10) with $Ud/\nu=100$ to calculate the bubble trajectories.

The vorticity contours and bubble positions, along with the pressure gradient field, at time $t=10$ are shown in Fig. 9 and for time $t=18$ in Fig. 10. In addition to the bubble positions, a solid line representing the the material line which was initially at the centerline is displayed. In Fig. 9, the shear layer is still predominantly parallel. During this parallel shear stage, the pressure gradients are small, and the bubbles closely follow the fluid elements. We see that the material line and edge of the bubble field correspond well here. However, at $t=18$, when the vortex is well developed, the material line and bubble field do not correspond as well. As expected, this difference is most pronounced where the pressure gradients are large, at the vortex center. In addition to the accumulation of bubbles at the vortex center, there is a depletion of bubbles all along the material line, even near the stagnation point between vortices, or in the "braid" region. This can also be explained in terms of the pressure gradients, even though the pressure gradients are weak in this region. For a bubble traveling parallel to the material line in the braid region, the vectors u and $-\nabla P$ are roughly colinear. Therefore, the bubble is being acted on by a uniform pressure gradient over a longer length scale than bubbles elsewhere in the flow.

The accumulation of bubbles into the vortex center can be measured by calculating the bubble concentration in circular shells around the vortex center. Such radial concentration profiles are shown at different times in Fig. 11. Here the concentration is calculated by sorting the bubbles
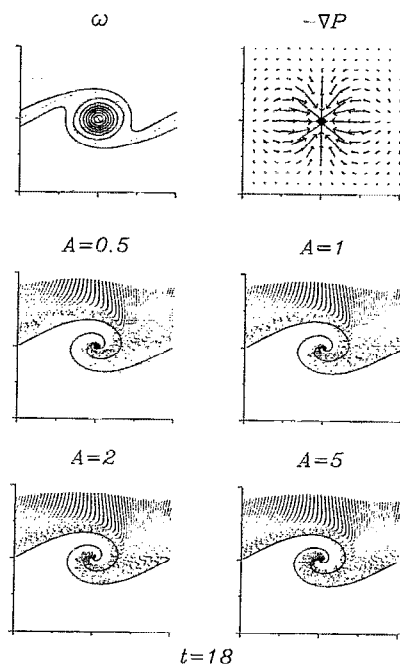
into 20 radial shells where the thickness of each shell is $\Theta_{ms}/10$. Using this method we obtain bubble concentrations above 100 times the initial concentration.

By measuring these radial concentration profiles, we can easily compare results in the shear layer calculation to those obtained in the isolated solid-body vortex. If we seed a solid-body vortex with a uniform bubble concentration
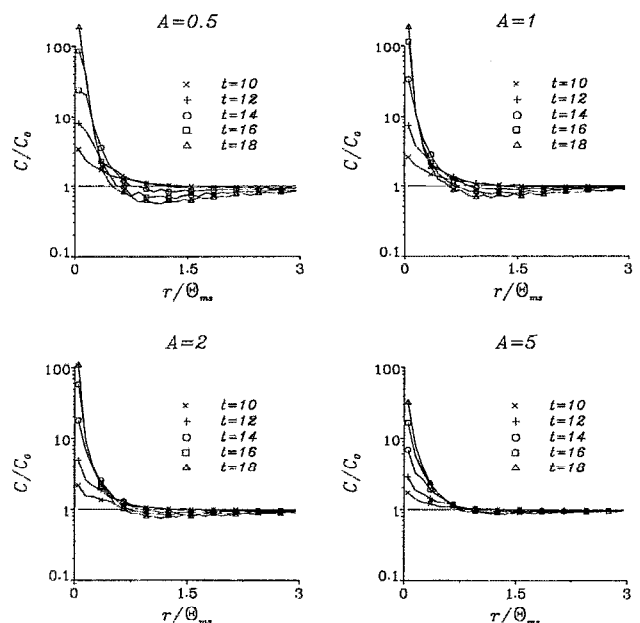

FIG. 11. Radial concentration profile for $A=0.5,1,2,5$ bubbles at various times. The radius is normalized by the maximum-slope thickness, Θ_{ms}.

2334   Phys. Fluids A, Vol. 5, No. 10, October 1993
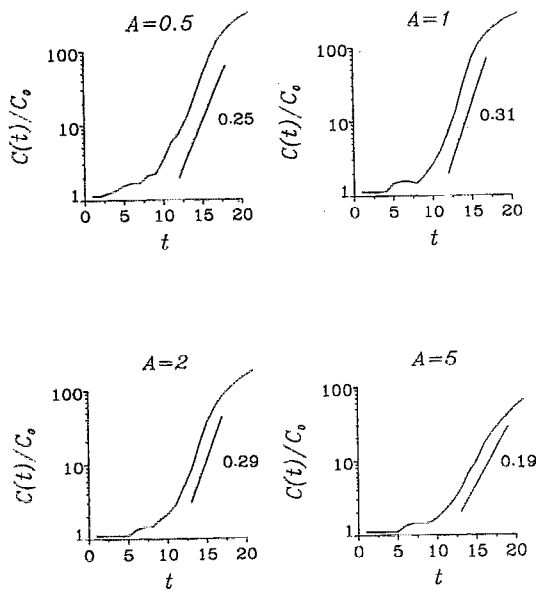
G. R. Ruetsch and E. Meiburg   2334

FIG. 12. Time series of the concentration in the innermost bin of Fig. 11. This bin corresponds to a radius of $\Theta_{ms}/10$. During the time when the vortex core exists, exponential growth is observed. The straight lines indicate the exponential growth in terms of 10^x.
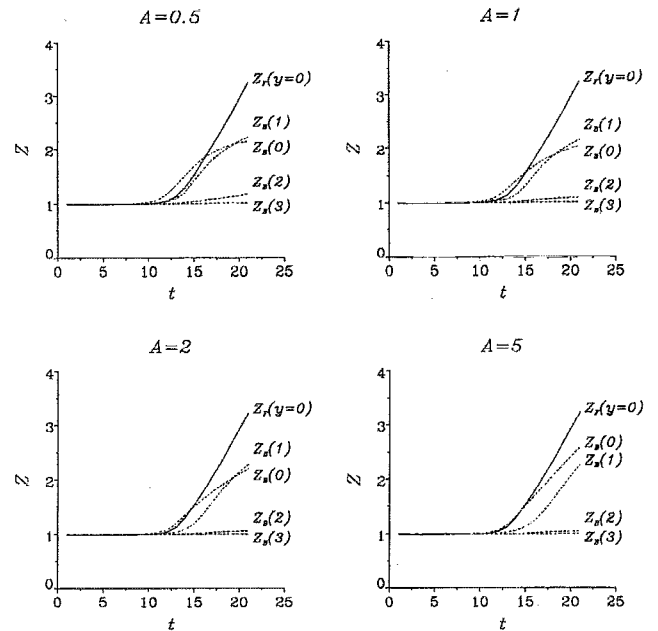

FIG. 13. Time series of Z for material elements and bubbles that are initially placed along the centerline. In addition, Z for bubbles introduced above the centerline is also shown.

C_0, then the concentration within some small circle about the vortex would grow exponentially for an exponential rate of entrapment. We therefore expect an exponential increase in bubble concentration about the vortex in the shear layer. The time series for the concentrations of the innermost bin from Fig. 11 are shown in Fig. 12. Here we see, after an initial period of slow growth during the parallel shear stage, an approximately exponential growth in the bubble concentration. In agreement with the solid-body case, we see that at an intermediate value of the inertia parameter there is an optimum growth rate in the concentration. After this exponential growth, the curves level off since the flow was only partially seeded with bubbles. The leveling off can be eliminated by either seeding bubbles further out or by using a smaller bin size.

In addition to the accumulation of bubbles in the vortex center, there are features of the bubble motion which are important in the context of mixing. One such characteristic concerns the effect of the fluid motion on the "interface" between regions of fluid seeded with bubbles and regions of fluid without bubbles. For our two-dimensional case, the growth of this "interface" takes the form of the arclength of bubbles along the centerline. Since the bubbles in the shear layer were introduced as a rectangular grid, we can also measure the growth of the arclength of bubbles at a variety of vertical locations. Due to the passive nature of the bubbles assumed in this study, the different layers of bubbles are not affected by one another, and therefore the results for an internal layer of bubbles would be the same as if this layer defined the "interface." In this way we can calculate the optimum vertical location of bubble injection which results in the maximum growth of the interface.

For Lagrangian elements, the arclength of a material line grows fastest when this line initially coincides with the centerline of the shear layer. We will compare our results for bubbles against the growth of this material line. The growth of the several bubble lines are plotted in Fig. 13 for the four different cases of the inertial parameter.

First we will consider the cases of the bubble lines which initially coincide with the centerline. The arclength of bubbles initially along the centerline, denoted by $Z_B(y=0)$, compared to the arclength of fluid or material elements initially along the centerline, denoted by $Z_F(y=0)$, is determined by two features which can be related to the bubble motion in a solid-body vortex, namely the accumulation of the bubbles in and the azimuthal bubble velocity about the center of the vortex. The accumulation of the bubbles into the vortex center causes the spiral structure of the bubble line to shrink, resulting in smaller values of Z_B/Z_F. From Fig. 1 we know that relative to fluid elements, the bubbles have a greater frequency about the vortex center, which tends to increase Z_B/Z_F. The importance of these two features depends on the value of the inertia parameter, A. However, for all values of A the long-term behavior is dominated by the accumulation factor, resulting in $Z_B/Z_F < 1$ observed at long times in Fig. 13. Also in agreement with Fig. 1 we observe that the final value of Z_B in Fig. 13 is smallest for the case where $A=1$, which corresponds to the largest accumulation rate observed in Fig. 12. We also see that regions where $Z_B/Z_F > 1$ occur near the beginning of the evolution of the vortex cores. From Fig. 1 we expect this to be most prominent at small A, which is confirmed by Fig. 13. The above features can be observed in the time series of bubble and fluid lines in Figs. 14 and 15. For the case where $A=5$, the
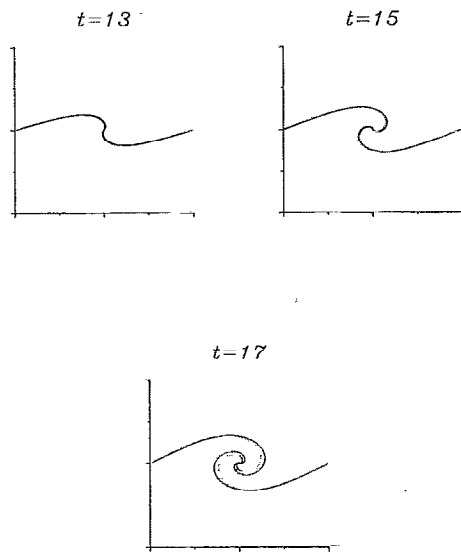
FIG. 14. Snapshot of material line (—) and bubble line ($\cdots$) at three different times for $A=5$. Both lines were initially placed on the centerline.

small difference between the fluid and bubble lines' wrapping about the vortex center is negligible compared to the effect of the entrapment of bubbles into the vortices. However, for $A=0.5$ in Fig. 15 the differential rotation rate is more pronounced, resulting in a larger Z for bubbles than fluid elements soon after the vortex center develops.

Although the accumulation of bubbles into the vortex center results in $Z_B(y=0)/Z_F(y=0)<1$, this same feature can cause the opposite behavior for lines away from the vortex center. This is seen in Fig. 13, where for the smaller inertia parameter cases $Z_B(y=1)>Z_B(y=0)$ at the final time step. In all cases, even the initially displaced bubble line cannot achieve a larger Z than the material line initially at the centerline.
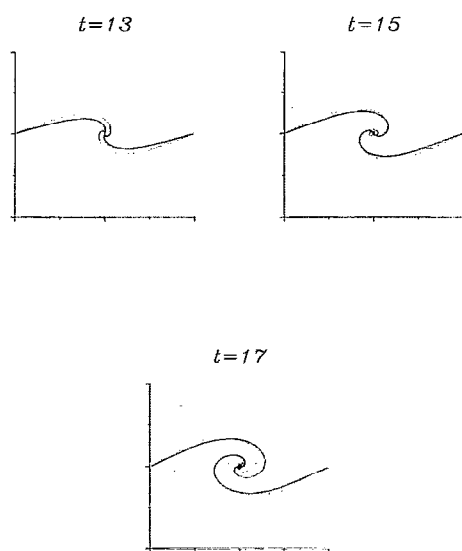

FIG. 15. Snapshot of material line (—) and bubble line ($\cdots$) at three different times for $A=0.5$.

C. Bubbles in a shear layer with gravity

In this section we now consider the effects of gravity on the entrapment and mixing characteristics of bubbles in a shear layer. This situation, where we combine gravitational effects and a finite vortex, is quite different than the situations discussed so far. The cases of an infinite solid-body vortex and a finite vortex without gravity guarantee that equilibrium points exist, and eventually all bubbles are captured at these equilibrium points. In this section, however, the existence and effectiveness of the equilibrium points needs to be established. Before we do this, the initial condition must be changed from the previous case to accommodate the effect of gravity and provide meaningful results. The initial conditions used in this case are to introduce the bubbles below the shear layer in a region where the flow field is roughly uniform and to give the bubble an initial velocity equal to that of the local fluid velocity plus the rise velocity, $\mathbf{W}$.

The ability of the fluid motion to capture bubbles introduced below the shear layer depends heavily on the stage of temporal development of the shear layer when the bubbles pass through the shear layer. As we have seen in the previous section, there is little effect of the shear layer on the bubbles when the flow is roughly parallel. It is only during the stages when the vortex core develops or has already developed that the bubble motion deviates from the fluid motion. The distance below the shear layer at which we introduce the bubbles then becomes an important parameter. To eliminate this parameter in our investigation, we will study the bubble motion in a steady flow. Although this can be done using static frames from the temporal shear layer above, a more efficient method is to use an analytical representation of the flow. Here we use a periodic row of Stuart vortices[21] for this purpose. Nondimensionalized by the maximum vorticity and the velocity difference between streams, the streamfunction for the Stuart vortices is

$$\psi=\frac{1}{4}\left(\frac{1+\rho}{1-\rho}\right)\ln\left[\cosh\left(2\frac{1-\rho}{1+\rho}y\right)-\rho\cos\left(2\frac{1-\rho}{1+\rho}x\right)\right],$$

(33)

where ρ is a parameter which can be used to represent the evolution of the shear layer. When $\rho=0$, Eq. (33) gives a parallel flow, and when $\rho=1$, Eq. (33) gives the solution to a periodic row of point vortices. The use of a time dependent ρ in Eq. (33) has been used by Meiburg and Newton[22] to model passive particle dynamics in a viscously decaying shear layer. Some analytical work concerning the motion of heavy particles and bubbles in steady Stuart vortices is reported in Tio *et al.*[23] In this study we will use $\rho=0.25$, which has been reported by Browand and Weidman[24] to represent the large-scale behavior of mixing layers, and has been used by Gañán-Calvo and Lasheras[25] to study heavy particle dynamics in a free shear layer. The streamfunction, velocity profile through the vortex center, and the initial randomly placed bubble locations are shown in Fig. 16. In order to obtain analytical features of the equilibrium points in the flow, we will not be using the drag correction factor applied in the case without gravity. How-
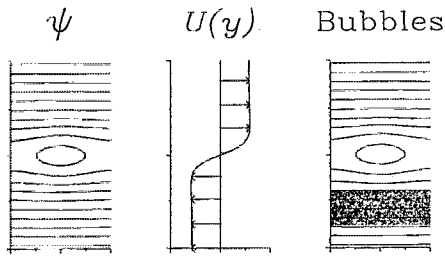
ψ   U(y)   Bubbles

FIG. 16. The streamfunction, velocity profile taken through the vortex center, and initial bubble locations for the simulation of bubble motion in a periodic row of Stuart vortices. The abscissa represents one period given by $l=\pi(1+\rho)/(1-\rho)$ where $\rho=0.25$, and the ordinate represents $2l$.

ever, as the previous section has shown, the effect of this drag correction did not qualitatively affect the results when compared to the results of the solid-body vortex without this factor.

We begin our analysis of bubble motion in a periodic row of Stuart vortices by examining the conditions under which equilibrium points exist. The existence of equilibrium points for bubbles in a Stuart vortex is discussed in detail by Tio et al.,[23] and here we only present a brief discussion. One can determine whether or not and where the equilibrium points lie by finding the solution to Eq. (5) with $d\mathbf{V}/dt=\mathbf{V}=0$. The solutions for the force balance in the x and y directions for various A and W are shown in Fig. 17. Here the dashed lines represent the points where the x-force equation is balanced, and the solid lines repre-
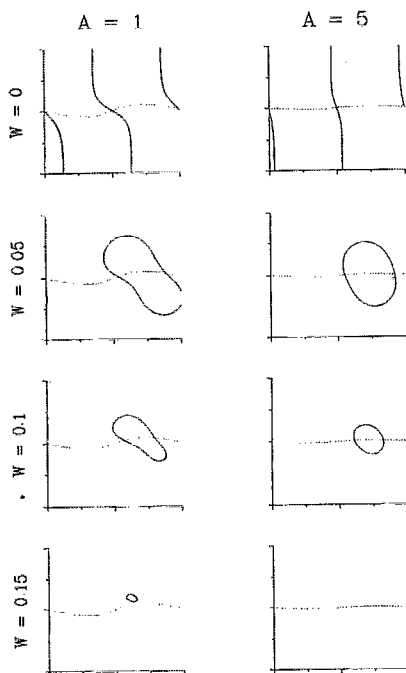
sent the points where the y-force equation is balanced. The intersections indicate the locations of the equilibrium points. For $W=0$ there are two equilibrium points, one at the stagnation point in the vortex center which is stable and one at the stagnation point in the braid region, which is unstable. As we increase W from zero, the lines associated with the y-force balance change and form a closed loop, and the intersections between this loop and the x-force balance line are displaced from the stagnation points. As W increases further, this loop becomes smaller and at some point disappears. Physically this corresponds to the case when there is no point in the flow where the combination of viscous and pressure forces can balance the gravitational effects. However, even before the y-momentum loop vanishes the equilibrium point can vanish, as indicated in the case where $W=0.15$ and $A=1$. Here there are no intersections and thus no equilibrium points, even though there are locations where the individual components are balanced separately. These situations, especially where the loci almost intersect, have an interesting effect on mixing, and will be discussed later.

Although the location of the equilibrium points is not given in closed form for this flow, we do observe similar trends to the case of the solid-body vortex. In both cases as W increases the equilibrium point moves away from the vortex center, and as A increases the vertical location of the equilibrium point is lower.

Now that we have discussed the existence of equilibrium points, we will examine the ability of these points to capture bubbles. We begin by looking at the effect of the inertia parameter on the entrapment of bubbles by the Stuart vortex. Several snapshots of bubble positions for various A and times and constant W are shown in Fig. 18. In the first row of Fig. 18 the average vertical bubble location is near the vortex center. In agreement with the previous sections, we find that at this time the population of bubbles in a small circle around the equilibrium point is largest for $A=1$ of the cases shown. For $A=0.5$ the bubbles near the equilibrium point "overshoot" the equilibrium point. However, in terms of the percentage of bubbles trapped by the vortex, the last time frame indicates that the smaller value of A traps the most bubbles. The ability of the vortex to capture bubbles is not determined by the motion of the bubbles near the equilibrium point, but rather the effect of the flow on the bubbles in the entire domain. The number of bubbles that are captured reflects the ability of the bubble velocity $\mathbf{V}$ to deviate from the fluid and rise velocities, $\mathbf{u}+\mathbf{W}$. This deviation is more pronounced for smaller values of A, resulting in the overall entrapment characteristic that the percentage of bubbles trapped increases with decreasing A. A plot of the total percentage of bubbles captured by the vortex for various A is shown in Fig. 19, where the effect of A on the capturing of bubbles is more clearly seen. This is done for several values of W. (Note: this does not imply that smaller bubbles are less likely to be captured. $A\sim 1/a^2$ but $W\sim a^2$, and the entrapment features are more sensitive to changes in W.) As expected, the larger W becomes the fewer bubbles are captured because the bubbles spend less time in a region influenced by the

A = 1   A = 5

W = 0

W = 0.05

W = 0.1

W = 0.15

FIG. 17. Equilibrium points in a Stuart vortex exist where the lines which represent the balanced forces in the x direction (···) and y direction (—) intersect. Note that for $W=0$ there is a stable equilibrium point at the stagnation point in the vortex center and an unstable equilibrium point at the stagnation point in the braid region. Each graph represents one period in each direction.
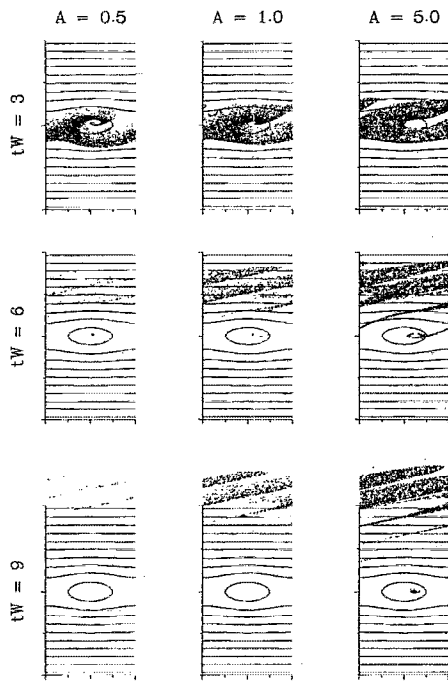
A = 0.5   A = 1.0   A = 5.0

tW = 3

tW = 6

tW = 9

FIG. 18. Bubble locations at different times for various A and $W=0.1$. Although the concentration in the first row about the equilibrium point is larger for $A=1.0$ than $A=0.5$, the percentage of captured bubbles at later times is larger for $A=0.5$. The abscissa represents l and the ordinate represents $2l$.

W = 0.05   W = 0.15   W = 0.2

tW = 3

tW = 9

FIG. 20. Bubble locations for different W and $A=1$. As expected, for $W=0.2$ no bubbles are trapped. At longer times, no bubbles are captured for $W=0.15$, however, the least unstable point in the flow efficiently retains bubbles and creates the line of bubbles emanating from this point.

vortex. This can be seen in Fig. 20, where A is held constant and W is the variable. Note that the times are scaled by W so that the bubbles with different W rising in a still fluid would travel the same vertical distance at a time tW. Once again, we see from the later time that the percentage of bubbles captured by the vortex increases with decreasing W.

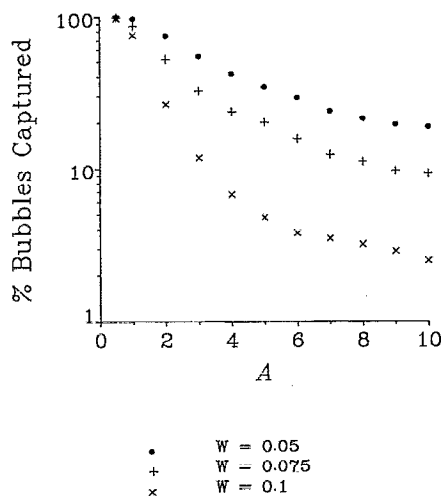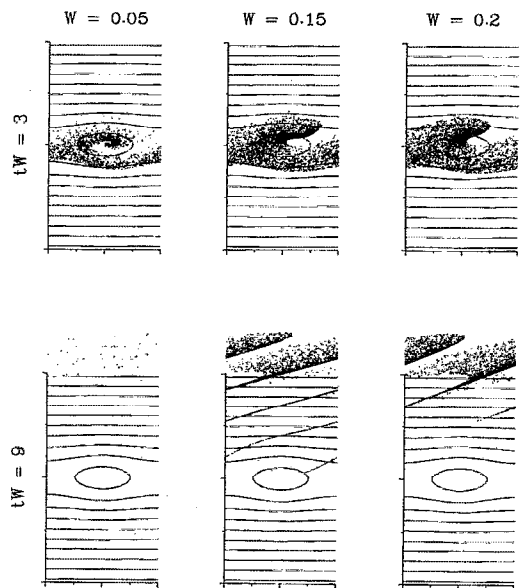From Fig. 20 we see that for $W=0.2$ no bubbles are trapped, in agreement with the results of Fig. 17. On the

other hand, from Fig. 20 one might conclude that for the case of $W=0.15$ some bubbles are captured, even though from Fig. 17 we know that the equilibrium point does not exist. In running the simulation further we do see that no bubbles are captured for $A=1$ and $W=0.15$. The loci in Fig. 17 are close enough, however, so that there is a significant restraining effect of bubbles. This restraining effect is responsible for the long streaks generated at this least unstable point. In the context of mixing, such points in the flow generate large interfaces between the flow seeded with bubbles and the flow without bubbles. If u_∞ is the freestream horizontal velocity and $\xi = W/u_\infty$, then the angle these bands make with the horizontal direction can be expressed as $\theta = \tan^{-1}(\xi)$ and the distance between these bands is given by $d = l\xi/\sqrt{1+\xi^2}$. The length of the bands depends on how close the loci in Fig. 17 are.

V. DISCUSSION AND CONCLUSIONS

In this paper we investigated the motion of small spherical bubbles in a variety of vortical flows. In particular, we are interested in describing the phenomenon of bubble accumulation in vortices.

In our initial investigation concerning bubble accumulation we utilize the solid-body vortex flow field. We find that the accumulation can be described by two features: the equilibrium point and the rate of entrapment of the bubbles into the equilibrium point. The location of the equilibrium point is a function of both the bubble rise velocity W and the inertia parameter A, and is located at the vortex center when $W=0$. Since the vortex extends to infinity, an equilibrium point exists for any combination of A and W. The rate of entrapment was found to depend only on A (assum-

FIG. 19. Percentage of bubbles captured versus A for different W in a Stuart vortex.

•   W = 0.05
+   W = 0.075
×   W = 0.1

ing the drag correction term, f_1, is not used), and more importantly was found to have an optimum value at some A.

We have also examined the motion of bubbles in a temporally evolving shear layer. Without gravitational effects we find that the bubbles accumulate in the vortex center, once it develops, which is consistent with the solid-body vortex model. We also find that the time series of the bubble concentration about the vortex center grows exponentially once the vortex core develops, and the trends in growth rates for different A agree with the rate of entrapment dependence on A for the solid-body vortex model.

We have modeled the bubble motion in a shear layer in the presence of gravity by using Stuart vortices. For this case, where we have a gravitational influence and finite vortex size, equilibrium points do not always exist. Even for cases when equilibrium points do exist, not all of the bubbles are captured by these points. The percentage of bubbles captured does not follow the trends in the rate of entrapment in the previous cases, where an optimum rate in terms of A is observed, but rather is determined by the ability of the bubbles to deviate from the local fluid and rise velocities. This ability is greatest when A is smallest, and therefore the largest percentage of bubbles captured by the vortex occurs when A is smallest.

The stretching of material and bubble lines was also examined in this study, which is useful in determining how bubbles can be injected into the flow so that the interface between the portion of the flow seeded with and without bubbles obtains the largest value. In all cases, the bubble interface is smaller than the material line initially placed on the centerline of the mixing layer. This reflects the dominance of the accumulation mechanism, which results in the spiral structure of the bubble interface being compressed towards the vortex center. However, due to the increased frequency of the bubbles about the vortex for small A, as the shear layer begins to form vortices the bubbles can temporarily achieve a larger interface than the material line.

Throughout this study, the accumulation of bubbles into equilibrium points is a repeated feature. Because of the predominance of this accumulation, we must comment on the violation of one of our assumptions due to this feature. As we have seen in the temporally evolving shear layer, the concentration in the vortex center can reach very high values, in which case the assumption of a dilute concentration of bubbles is violated. Therefore, to accurately represent the bubble and fluid flows at the latter stages, one would have to account for the effect of the bubbles on each other and the fluid.

ACKNOWLEDGMENTS

APPENDIX: BUBBLE SIMULATION SCHEME AND ACCURACY

In this section we discuss the method for calculating particle trajectories, where the particle acceleration dV/dt is given by Eq. (5):

$$\frac{d\mathbf{V}}{dt} = A(\mathbf{u} + \mathbf{W} - \mathbf{V}) + R\left(\frac{D\mathbf{u}}{Dt} + \frac{1}{2}\frac{d\mathbf{u}}{dt}\right). \quad (A1)$$

Since we are concerned with the particle location and not only the particle velocity, Eq. (5) actually represents a system of two ODE's, the first being Eq. (5) and the second

$$\frac{d\mathbf{Y}}{dt} = \mathbf{V}. \quad (A2)$$

The method used here to solve Eqs. (5) and (A2) is a second-order predictor–corrector method. The predictor step uses a first-order forward Euler scheme:

$$\mathbf{V}^{n+1*} = \mathbf{V}^n + \left(\frac{d\mathbf{V}}{dt}\right)^n \Delta t,$$

$$\mathbf{Y}^{n+1*} = \mathbf{Y}^n + \mathbf{V}^n \Delta t, \quad (A3)$$

and the trapezoidal rule is applied during the corrector step:

$$\mathbf{V}^{n+1} = \mathbf{V}^n + \frac{\Delta t}{2}\left[\left(\frac{d\mathbf{V}}{dt}\right)^n + \left(\frac{d\mathbf{V}}{dt}\right)^{n+1*}\right],$$

$$\mathbf{Y}^{n+1} = \mathbf{Y}^n + \frac{\Delta t}{2}(\mathbf{V}^n + \mathbf{V}^{n+1*}). \quad (A4)$$

The application of Eqs. (36) and (37) in general is straightforward, but we have yet to determine how the particle acceleration, Eq. (5), is approximated. The computational form of Eq. (5) is relatively simple:

$$\left(\frac{d\mathbf{V}}{dt}\right)^n = A(\mathbf{u}_{\mathbf{Y}^n}^n + W - \mathbf{V}^n) + R\left[\left(\frac{D\mathbf{u}}{Dt}\right)^n_{\mathbf{Y}^n} + \frac{1}{2}\left(\frac{d\mathbf{u}}{dt}\right)^n_{\mathbf{Y}^n}\right],$$

$$\left(\frac{d\mathbf{V}}{dt}\right)^{n+1*} = A(\mathbf{u}_{\mathbf{Y}^{n+1*}}^{n+1} + \mathbf{W} - \mathbf{V}^{n+1*}) + R\left[\left(\frac{D\mathbf{u}}{Dt}\right)^{n+1}_{\mathbf{Y}^{n+1*}}\right.$$

$$\left. + \frac{1}{2}\left(\frac{d\mathbf{u}}{dt}\right)^{n+1}_{\mathbf{Y}^{n+1*}}\right], \quad (A5)$$

however, the problem arises in approximating the fluid velocity derivatives, $(D\mathbf{u}/Dt)$ and $(d\mathbf{u}/dt)$. The goal here is to obtain overall a second-order accurate particle tracking scheme, as is done with the vortex blob evolution, with the minimum computational effort. In a steady flow field, one can take an arbitrarily small time step to calculate these terms. For unsteady flows, as is the case here, one would have to advance the flow field to this intermediate step in order to take into account the temporal effect on these fluid derivatives. It would be more efficient to utilize the existing flow-field data.

Since a corrector step is applied to the derivatives in Eq. (37), first-order accurate estimates of $(D\mathbf{u}/Dt)$ and

(du/dt) should yield the desired overall accuracy, although these first order schemes must be chosen carefully. Using a forward Euler scheme for both the n and $n+1^*$ steps, as well as a backward Euler scheme for both steps results in an overall first order scheme. However, if at the nth step we use a forward Euler scheme:

$$\left(\frac{D\mathbf{u}}{Dt}\right)^n_{\mathbf{Y}^n} = (\mathbf{u}^{n+1}_{(\mathbf{Y}^n + \mathbf{u}^n_{\mathbf{Y}^n}\Delta t)} - \mathbf{u}^n_{\mathbf{Y}^n})/\Delta t,$$

$$\left(\frac{d\mathbf{u}}{dt}\right)^n_{\mathbf{Y}^n} = (\mathbf{u}^{n+1}_{(\mathbf{Y}^n + \mathbf{V}^n\Delta t)} - \mathbf{u}^n_{\mathbf{Y}^n})/\Delta t, \qquad \text{(A6)}$$

and at the $n+1^*$-st step a backward Euler scheme:

$$\left(\frac{D\mathbf{u}}{Dt}\right)^{n+1}_{\mathbf{Y}^{n+1*}} = (\mathbf{u}^{n+1}_{\mathbf{Y}^{n+1*}} - \mathbf{u}^n_{(\mathbf{Y}^{n+1*} - \mathbf{u}^{n+1}_{\mathbf{Y}^{n+1*}}\Delta t)})/\Delta t$$

$$\left(\frac{d\mathbf{u}}{dt}\right)^{n+1}_{\mathbf{Y}^{n+1*}} = (\mathbf{u}^{n+1}_{\mathbf{Y}^{n+1*}} - \mathbf{u}^n_{(\mathbf{Y}^{n+1*} - \mathbf{V}^{n+1*}\Delta t)})/\Delta t, \qquad \text{(A7)}$$

then the overall scheme is second order. In calculating each fluid derivative, note that the velocities must be evaluated along a single particle/fluid path at both $n+1^*$-st and nth time.

In this section we prove the second-order accuracy of the scheme discussed above. We will do this for the equation:

$$\frac{dV}{dt} = R\left(\frac{Du}{Dt} + \frac{1}{2}\frac{du}{dt}\right), \qquad \text{(A8)}$$

where the viscous/inertial terms in Eq. (5) are left out since the accuracy for these terms is straightforward. In this section we will abbreviate our notation by dropping any n superscripts and Y^n subscripts, and also use the subscripts x and t to indicate differentiation, with respect to space and time. Also, u^* represents u at step $n+1$ and location Y^{n+1*}. We will only consider one dimension in space.

To begin the analysis we first determine the $n+1$-st particle velocity in terms of a Taylor series about the nth time step:

$$V^{n+1} = V^n + R\Delta t\left(u_t + uu_x + \frac{1}{2}(u_t + Vu_x)\right)$$

$$+ R\frac{(\Delta t)^2}{2}\left(u_{tt} + u_t u_x + (u+V)u_{xt} + V(u_x)^2 \right.$$

$$\left. + Vuu_{xx} + \frac{1}{2}(u_{tt} + V_t u_x + 2Vu_{xt} + V^2 u_{xx})\right) + O(\Delta t^3). \qquad \text{(A9)}$$

In order for our numerical scheme to be second-order accurate, the scheme must reproduce the terms in Eq. (A9). In order to do this we must obtain approximations to the velocities in Eqs. (A6) and (A7) in terms of Taylor series about $u^n_{Y^n}$. Up to second order, the expressions for Du/Dt are

$$u^{n+1}_{Y^n + u\Delta t} \sim u + \Delta t(u_t + uu_x) + \frac{\Delta t^2}{2}(u_{tt} + 2uu_{xt} + u^2 u_{xx}), \qquad \text{(A10)}$$

$$u^{n+1}_{Y^{n+1*}} \sim u + \Delta t(u_t + Vu_x) + \frac{\Delta t^2}{2}(u_{tt} + 2Vu_{xt} + V^2 u_{xx}), \qquad \text{(A11)}$$

$$u^n_{(Y^{n+1*} - u^*\Delta t)} \sim u + \Delta t(Vu_x - uu_x)$$

$$+ \frac{\Delta t^2}{2}[-2u_x u_t - 2Vu_x^2 - 2Vuu_{xx}$$

$$+ (V^2 + u^2)u_{xx}] \qquad \text{(A12)}$$

and for du/dt are

$$u^{n+1}_{Y + V\Delta t} \sim u + \Delta t(u_t + Vu_x) + \frac{\Delta t^2}{2}(u_{tt} + 2Vu_{xt} + V^2 u_{xx}), \qquad \text{(A13)}$$

$$u^n_{(Y^{n+1*} - V^{n+1*}\Delta t)} \sim u - \Delta t^2(V_t u_x). \qquad \text{(A14)}$$

Substituting these expressions into Eqs. (A6) and (A7) we obtain the following expressions for the derivatives:

$$\left(\frac{Du}{Dt}\right)^n_{Y^n} \sim u_t + uu_x + \frac{\Delta t}{2}(u_{tt} + 2uu_{xt} + u^2 u_{xx}), \qquad \text{(A15)}$$

$$\left(\frac{Du}{Dt}\right)^{n+1}_{Y^{n+1*}} \sim u_t + uu_x + \frac{\Delta t}{2}(u_{tt} + 2Vu_{xt} + 2u_x u_t$$

$$+ 2Vu_x^2 + 2Vuu_{xx} - u^2 u_{xx}), \qquad \text{(A16)}$$

$$\left(\frac{du}{dt}\right)^n_{Y^n} \sim u_t + Vu_x + \frac{\Delta t}{2}(u_{tt} + 2Vu_{xt} + V^2 u_{xx}), \qquad \text{(A17)}$$

$$\left(\frac{du}{dt}\right)^{n+1}_{Y^{n+1*}} \sim u_t + Vu_x + \frac{\Delta t}{2}(u_{tt} + 2Vu_{xt} + V^2 u_{xx}$$

$$+ 2V_t u_x). \qquad \text{(A18)}$$

Note that the derivative approximations are only first-order accurate, however, when substituted into Eq. (A4) we obtain the Taylor series of Eq. (A9), which implies an overall second-order accurate scheme.

[1] B. J. Lázaro and J. C. Lasheras, "Particle dispersion in the developing free shear layer. Part 1. Unforced flow," J. Fluid Mech. **235**, 143 (1992).

[2] B. J. Lázaro and J. C. Lasheras, "Particle dispersion in the developing free shear layer. Part 2. Forced flow," J. Fluid Mech. **235**, 179 (1992).

[3] J. N. Chung and T. R. Troutt, "Simulation of particle dispersion in an axisymmetric jet," J. Fluid Mech. **186**, 199 (1988).

[4] M. R. Maxey and J. J. Riley, "Equation of motion for a small rigid sphere in a nonuniform flow," Phys. Fluids **26**, 883 (1983).

[5] T. R. Auton, J. C. R. Hunt, and M. Prud'homme, "The force exerted on a body in inviscid unsteady non-uniform rotational flow," J. Fluid Mech. **197**, 241 (1988).

[6] M. R. Maxey and S. Corrsin, "Gravitational settling of aerosol particles in randomly oriented cellular flow fields," J. Atmos. Sci. **43**, 1112 (1986).

[7] M. R. Maxey, "The motion of small spherical particles in a cellular flow field," Phys. Fluids **30**, 1915 (1987).

[8] K.-K. Tio and J. C. Lasheras, "The dynamics of a small spherical

2340   Phys. Fluids A, Vol. 5, No. 10, October 1993

G. R. Ruetsch and E. Meiburg   2340

particle in a modified Rankine vortex flow under the influence of gravity," submitted to Phys. Fluids A.

[9]J. C. R. Hunt, T. R. Auton, K. Sene, N. H. Thomas, and R. Kowe, "Bubble motion in large eddies and turbulent flows," in *Proceedings of the Conference on Transient Phenomena in Multiphase Flow* (Hemisphere, Belgrade, Yugoslavia, 1988), p. 103.

[10]N. H. Thomas, T. R. Auton, K. Sene, and J. C. R. Hunt, "Entrapment and transport of bubbles by transient large eddies in multiphase turbulent shear flows," in *International Conference on the Physical Modeling of Multiphase Flow* (BHRA Fluid Engineering, Cranfield, England, 1983), p. 169.

[11]R. Clift, J. R. Grace, and M. E. Weber, in *Bubbles, Drops, and Particles* (Academic, New York, 1978).

[12]P. G. Saffman, "The lift on a small sphere in a slow shear flow," J. Fluid Mech. **22**, 385 (1965).

[13]F. P. Bretherton, "The motion of rigid particles in a shear flow at low Reynolds number," J. Fluid Mech. **14**, 284 (1962).

[14]R. Mei, C. J. Lawrence, and R. J. Adrian, "Unsteady drag on a sphere at finite Reynolds number with small fluctuations in the free-stream velocity," J. Fluid Mech. **233**, 613 (1991).

[15]M. R. Maxey, "On the advection of spherical and non-spherical particles in a non-uniform flow," Philos. Trans. R. Soc. London Ser. A **333**, 289 (1990).

[16]G. K. Batchelor, in *An Introduction to Fluid Dynamics* (Cambridge University Press, Cambridge, 1967).

[17]B. J. Lázaro and J. C. Lasheras, "Particle dispersion in a turbulent, plane, free shear layer," Phys. Fluids A **1**, 1035 (1989).

[18]A. Leonard, "Vortex methods for flow simulation," J. Comput. Phys. **37**, 289 (1980).

[19]Y. Nakamura, A. Leonard, and P. Spalart, "Vortex simulation of an inviscid shear layer," AIAA Paper No. AIAA-82-0948, 1982.

[20]A. Michalke, "On the inviscid instability of the hyperbolic-tangent velocity profile," J. Fluid Mech. **19**, 543 (1964).

[21]J. T. Stuart, "On finite amplitude oscillations in laminar mixing layers," J. Fluid Mech. **29**, 417 (1967).

[22]E. Meiburg and P. K. Newton, "Particle dynamics and mixing in a viscously decaying shear layer," J. Fluid Mech. **227**, 211 (1991).

[23]K.-K. Tio, A. Liñán, J. C. Lasheras, and A. M. Gañán-Calvo, "On the dynamics of buoyant and heavy particles in a periodic Stuart vortex flow," J. Fluid Mech. (to be published, 1993).

[24]F. K. Browand and P. D. Weidman, "Large scales in the developing mixing layer," J. Fluid Mech. **76**, 127 (1976).

[25]A. M. Gañán-Calvo and J. C. Lasheras, "The dynamics and mixing of small spherical particles in a plane, free shear layer," Phys. Fluids A **3**, 1207 (1991).